Viktor Hofmann*, Gleb Kleyman and Jens Twiefel

Modeling and Experimental Investigation of a Periodically Excited Hybrid Energy-Harvesting Generator

Abstract: In this article the modeling of a broadband energy harvester utilizing piezoelectric and electromagnetic effects for rotational applications is presented. The hybrid energy harvester consists of a one-side-clamped piezoelectric bimorph with a solenoid on the free end and is excited periodically but non-harmonically by magnets that are fixed on a rotating object. To estimate and describe the performance of the energy harvester concept a linear semi-analytical model for the bimorph and the solenoid is developed and then enhanced for non-harmonic system oscillations by decomposing them into their harmonic components. A comparison between the calculated and measurement signals of a prototype device shows great conformity. According to model-based and experimental analysis, the hybrid system has good broadband behavior regarding electric power output. That aspect makes the device a perfect energy-harvesting system for application with highly fluctuating revolution speeds like miniature wind turbines.

Keywords: energy harvester model, piezoelectric, electromagnetic, transfer matrix method, non-harmonic oscillation

DOI 10.1515/ehs-2014-0043

Introduction – State of the Art

Hybrid energy-harvesting concepts are moving progressively into the focus of research, as these concepts provide an increase of performance and scope of energy-harvesting applications. One hybrid energy-harvesting concept for rotating applications utilizing piezoelectric and electromagnetic effects is specified in recent publications by Wurz, Kleyman, and Twiefel (2013). This article is focused on the modeling approach of this system. Introductorily an overview is given about the current situation of piezoelectric, electromagnetic and hybrid energy-harvesting concepts.

For the piezoelectric and also for the electromagnetic effect the excitation may be either translational or rotational. It depends on the application environment which form of kinetic energy is available. While piezoelectric and electromagnetic bending beam concepts are more common for vibrational excitation, electromagnetic rotor/stator combinations are used for rotating applications. Furthermore, there are a number of energy-harvesting systems that convert rotational motion into translational excitation forces and vice versa. Those serve as an inspiration for the hybrid concept presented in the following section.

Typical vibration-based energy-harvesting systems operate at their resonance frequency. Roundy and Wright (2004) present a piezoelectric generator based on a two-layer piezoelectric bending element with a tip mass (Figure 1–1). During vibration, the piezoelectric layers are compressed and elongated alternately. Thus an electric charge is getting induced. In resonance the relative motion between tip and base and consequently the electric power output is at the maximum. Beeby et al. (2007) show an energy-harvesting concept with a passive bending element and a solenoid attached at the tip of the element. During oscillation the solenoid is passing a permanent magnet, in this way a voltage is induced (Figure 1–2). Xing et al. (2009) propose a slightly different concept for an electromagnetic harvester. The bending element is made of high-permeability material and is mounted along the axial direction inside a solenoid. Two magnets with opposed magnetization are aligned outside of the solenoid. When the element vibrates its tip passes the magnets and the magnetization in the beam is reversed, thereby a voltage is induced inside the solenoid (Figure 1–3). Challa et al. (2008) developed a tunable piezoelectric bending type energy harvester. A pair of permanent magnets is placed up- and downside at the tip of a piezoelectric bending element. A second pair of magnets is attached to the

***Corresponding author: Viktor Hofmann,** Institute of Dynamics and Vibration Research, Leibniz Universität Hannover, Appelstr. 11, Hannover 30159, Germany, E-mail: hofmann@ids.uni-hannover.de
Gleb Kleyman: E-mail: gleb.kleyman@gmail.com, **Jens Twiefel:** E-mail: twiefel@ids.uni-hannover.de, Institute of Dynamics and Vibration Research, Leibniz Universität Hannover, Appelstr. 11, Hannover 30159, Germany

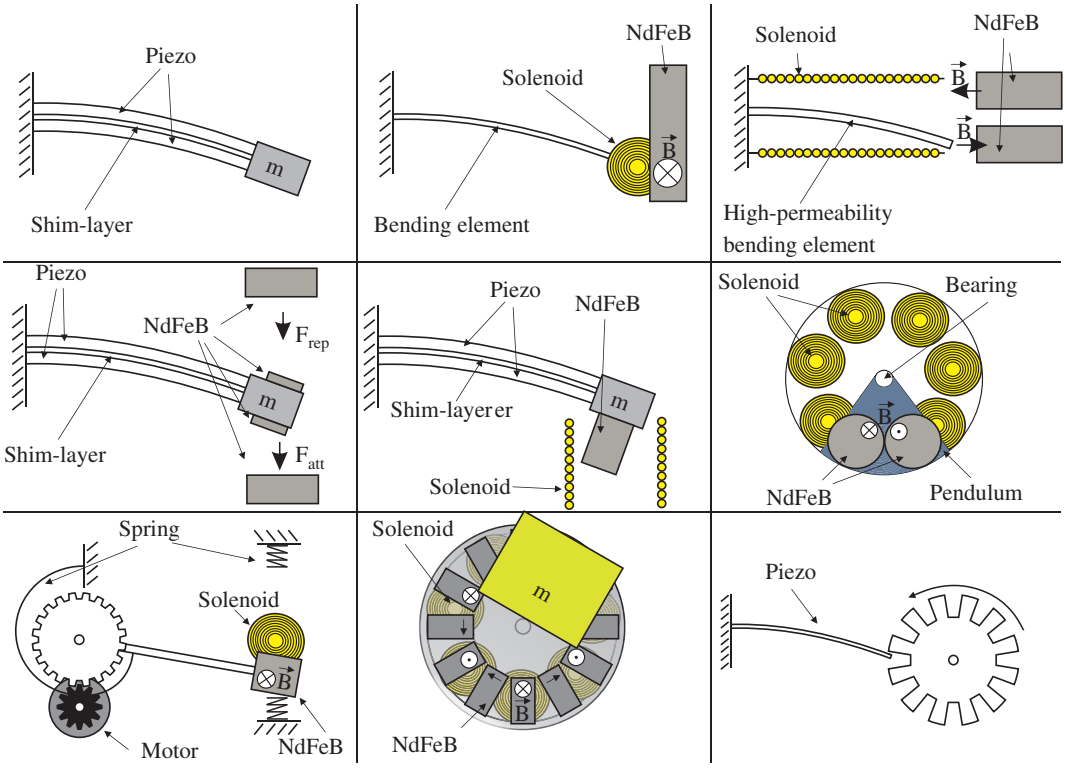

Figure 1: Functional principles of representative energy-harvesting systems.

inertial frame. Between the tip- and frame-magnets there are repulsive and attractive forces. By changing the distance between those magnet pairs the resonance frequency can be tuned (Figure 1–4). Challa, Prasad, and Fisher (2009) published a hybrid energy-harvesting system which combines principles of Roundy and Wright (2004) and Beeby, Tudor, and White (2006). A piezoelectric bending element has a permanent magnet at the tip. When the beam is vibrating the magnet dips inside a solenoid (Figure 1–5). Thus one energy source is used by two energy converters at once. A non-resonant power converter for translational excitations was presented by Spreemann et al. (2006). The energy harvester consists of a rotor and a stator. The rotor is a pendulum and rotates excited by vibrations. Two anti-parallel poled magnets are attached to the pendulum. The alternating magnetic field induces a voltage in an array of solenoids, which are arranged in a circle at the stator (Figure 1–6). Jung et al. (2013) designed a system that also converts vibration energy into rotation. Similar to Beeby, Tudor, and White (2006), a permanent magnet is attached at the tip of a cantilever beam. The base of the beam is connected to a gearing. When the beam is moving its tip passes a solenoid and the gearing revolves. A simple dynamo is linked to the gearing, thus a voltage is induced not only inside the solenoid but also by the dynamo (Figure 1–7).

There are also energy-harvesting concepts that convert energy directly from a rotational source. Wang, Shen, and Chen (2012) show a wideband electromagnetic harvester for tire pressure monitoring systems. That harvesting device is very similar to Spreemann et al. (2006). Permanent magnets are attached to an unbalanced rotor. Gravitation causes the rotor to rotate above a stator with an array of coils (Figure 1–8). A piezoelectric energy harvester for rotating energy sources was published by Priya (2005). An array of 12 piezoelectric bending elements is arranged along the circumference of a rotor shaft. A camshaft gear mechanism generates the torque to excite the elements (Figure 1–9). In this scenario a windmill is used as rotation energy source. This concept is picked up by Bressers et al. (2011). In their device the bending elements are exited contactless by magnetic forces. A series of magnets with alternating polarity is mounted on the rotating shaft. There are also magnets mounted on the tips of the bending elements. Rotation of the shaft induces a harmonic vibration into the piezoelectric elements via an alternating attractive/repulsive force between the magnet pairs. Their new approach is minimizing frictional losses and thus the device is more suitable for low wind speeds. Karami, Farmer, and Inman (2012) propose a piezoelectric wind turbine concept which is excited by non-harmonically magnetic forces and develop a semi-analytical model for this system.

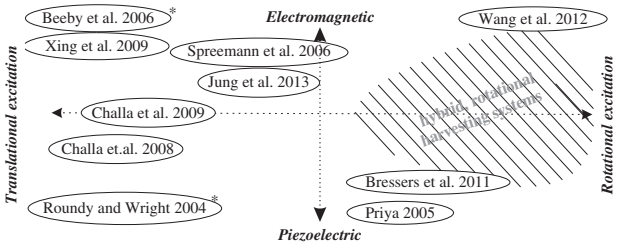

Figure 2: Classification of different types of energy-harvesting devices.
Note: *Exemplary for a large amount of publications on this principle.

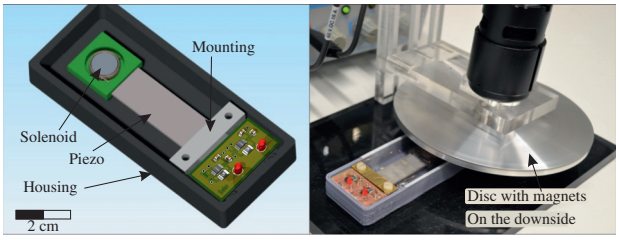

Figure 3: Concept CAD model and photography of the energy-harvesting device and testing rig.

Figure 2 shows a classification for the presented energy-harvesting concepts addicted to their physical energy conversion effect and the type of excitation. The vibration-based energy-harvesting systems are well developed. There are many different electromagnetic concepts and some piezoelectric devices are even on the market. The concepts by Priya (2005) and Bressers et al. (2011) show how the piezoelectric effect can also be utilized for rotating applications however electromagnetic concepts are more well established. Until now hybrid concepts are only studied for translational excitation, there is no hybrid rotational concept published. Our introduced hybrid energy-harvesting system fills this gap.

In the following the energy-harvesting concept is presented (section "Concept of a Hybrid Piezoelectric and Electromagnetic Energy Harvester"). The main part of this article deals with the description of the prototype unit by an analytical modeling approach (section "Modeling"). The model considers not only the properties of the solenoid and of the piezoelectric bimorph also the non-harmonically electromagnetic excitation forces. Furthermore, the analytical results are compared to the measurements of the prototype unit and the wideband performance of the concept is estimated (section "Analysis").

Concept of a Hybrid Piezoelectric and Electromagnetic Energy-Harvester

The following concept is based on the idea of a rotational piezoelectric energy harvester by Bressers et al. (2011). This magnetically driven piezoelectric harvester is extended by a solenoid with a ferromagnetic core on the tip.

The device is excited by four magnets attached to a rotating aluminum disc as shown in Figure 3. The attractive force between magnets and core material initiates a bimorph oscillation. Simultaneously the magnetic flux gradient induces a voltage in the solenoid. The total volume of the piezoelectric bimorph is 0.75 cm^3 and the solenoid has core diameter of 1 cm. The solenoid is bonded to the tip of the bimorph whereas the other end of the bimorph is clamped as shown in Figures 3 and 4. The bimorph is a typical resonant piezoelectric bending element and therefore it reaches the maximum electric power output related to the mechanical excitation power at its resonance frequency. Whereas the power output of the solenoid is quadratic to the applied mechanical power and thus to the revolution speed. By combination of both transducers in one unit a broadband energy-harvesting device is build. At low excitation speeds and high electric loads the piezoelectric part supplies the bigger part of electric energy. With increasing frequencies the power output of the solenoid grows and rises above the piezoelectric part. Thus such an energy-harvesting system may be used in an environment with highly fluctuating rotational speeds such as miniature wind turbines.

On the experimental setup (Figure 4) the disc is powered by an electric motor. Thereby the electric output variables (voltage and current) are measured for different electric load-resistance and different revolution speeds by a digital oscilloscope. Measurements have shown, that the magnetic attraction force leads to a non-harmonic excitation. Karami, Farmer, and Inman (2012) proposed how the non-harmonic excitation of the bimorph can be simulated by discretization and numerical integration of the nonlinear equation of motion. Nevertheless we want to submit an analytical modeling approach in the next section.

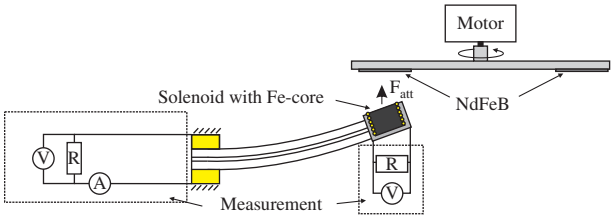

Figure 4: Layout of the experimental setup.

Modeling

In this section linear analytical models for the piezoelectric bimorph (section "Analytical Model of a Piezoelectric Parallel Bimorph for Steady-State, Harmonic Vibrations") and for the solenoid (section "Electromagnetic Solenoid") of the hybrid energy harvester are presented.

The model for the bimorph applies to steady-state and harmonic system oscillations. However, it is assumed that the energy harvester is excited non-harmonically by the magnetic force. In order to take even non-harmonic system behavior into account, the non-harmonic input variables are decomposed into their harmonic components. Using the model harmonic system responses are calculated from each harmonic input variable and then composed to one non-harmonic response (section "Non-harmonic Excitation Force Applied to Linear Oscillating Systems").

Analytical Model of a Piezoelectric Parallel Bimorph for Steady-State, Harmonic Vibrations

For many practical applications including the bending converter only the behavior at the element boundaries matters. The transfer-matrix method as described by Pestel and Leckie (1963) picks up on this circumstance by approaching the behavior of a device with simple matrix algebra for specific degrees of freedom. Thus, the method offers compared to a finite element method (FEM) calculation a reduced computation time as well as simple and flexible investigation of load influences. To apply the method to our application, it is necessary to derivate a transfer matrix for the used piezoelectric bending transducers.

For the bending converter the mechanical state variables – velocity v, angular velocity $\dot{\varphi}$, bending moment M and force F– at the two boundaries of the bending actuator and the electric variables – voltage U and current I– are considered and linked by the transfer matrix $\boldsymbol{A}$:

$$\begin{pmatrix} v_2 \\ \dot{\varphi}_2 \\ M_2 \\ F_2 \\ I \end{pmatrix} = \mathrm{A} \begin{pmatrix} v_1 \\ \dot{\varphi}_1 \\ M_1 \\ F_1 \\ U \end{pmatrix} \quad [1]$$

The subscript "1" indicates the end of the element at $x = 0$ and the subscript "2" represent the end at $x = l$ with l as the element length (Figure 5). In the presented model steady-state, harmonic vibrations with the excitations frequency ω are assumed. Therefore, the boundary conditions can be expressed as complex quantities with the respective phase angle $\psi_{(*)}$ and the respective amplitudes $|*|$:

$$\begin{pmatrix} v_1 \\ \dot{\varphi}_1 \\ M_1 \\ F_1 \\ U \end{pmatrix} = \begin{pmatrix} |v_1|e^{j\omega t+j\psi_{v_1}} \\ |\dot{\varphi}_1|e^{j\omega t+j\psi_{\dot{\varphi}_1}} \\ |M_1|e^{j\omega t+j\psi_{M_1}} \\ |F_1|e^{j\omega t+j\psi_{F_1}} \\ |U|e^{j\omega t+j\psi_U} \end{pmatrix} \quad \begin{pmatrix} v_2 \\ \dot{\varphi}_2 \\ M_2 \\ F_2 \\ I \end{pmatrix} = \begin{pmatrix} |v_2|e^{j\omega t+j\psi_{v_2}} \\ |\dot{\varphi}_2|e^{j\omega t+j\psi_{\dot{\varphi}_2}} \\ |M_2|e^{j\omega t+j\psi_{M_2}} \\ |F_2|e^{j\omega t+j\psi_{F_2}} \\ |I|e^{j\omega t+j\psi_I} \end{pmatrix} \quad [2]$$

The resulting 5×5-transfer-matrix $\boldsymbol{A}$ depends on the transducer geometry, its material and the excitation frequency. Its determination is based on physical models, in our case on the basis of the well-established Euler-Bernoulli beam theory. For simplicity the theory is valid for small deformations assumes linear-elastic material properties and neglects the effect of transverse shear and the rotary inertia. While applying the beam model to the bimorph besides the piezoelectric coupling the multilayer aspect has to be taken into account.

Definition of the Bimorph

The used piezoelectric bimorph consists of two identical piezoelectric layers (height h_p) and one conductive

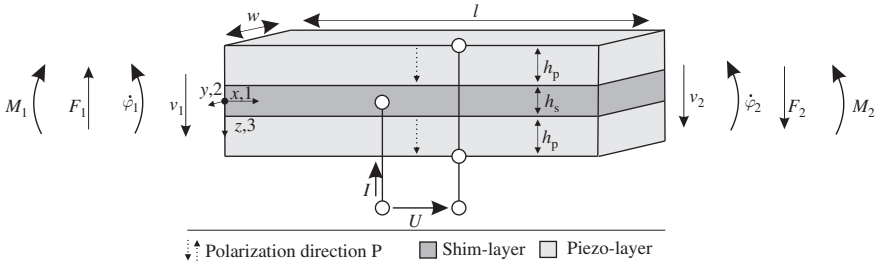

Figure 5: Boundary values of a bimorph.

passive middle shim layer (height h_s). The two piezoelectric layers have the same polarization direction P and are driven in an electric parallel connection (*parallel bimorph*), see Figure 5. If an electric potential is applied on the bimorph, one of the piezoelectric layer extends and the other shortens in the longitudinal direction. This results in a bending of the bimorph. Conversely a bending leads to the generation of an electric potential. To describe the material behavior of the middle shim the Hooke's law is sufficient (In the following equations the index s indicates the properties of the middle shim layer.):

$$S_{1,s} = s_{11,s} T_{1,s} \tag{3}$$

Whereas in the description of the material behavior of the piezoelectric layers the following linear piezoelectric material laws are adopted (IEEE [1987]):

$$S_1 = s_{11}^{E} T_1 + d_{31} E_3 \tag{4}$$

$$D_3 = d_{31}^{E} T_1 + \varepsilon_{33}^{T} E_3 \tag{5}$$

These relationships apply only to small mechanical and electrical amplitudes of a piezoelectric oscillator in the case that all stresses beside the stress in longitudinal direction T_1 are assumed to be zero. The linear dependencies between the mechanical strain S_1, the mechanical stress T_1, the dielectric charge displacement D_3 and the electric field strength E_3 are described by the constants d_{31} for the piezoelectric constant, s_{11}^{E} for the elastic compliance under the condition of a constant electric field and the dielectric constant ε_{33}^{T} at constant stress. The electric field strength E_3 for the parallel bimorph can also be expressed as a function of voltage U:

$$E_3 = \frac{U}{h_p} \tag{6}$$

Kinematic Linearization

Ensuing from small displacements the kinematics of the bimorph can be simplified by a geometric linearization. Figure 6 illustrates the linear kinematics of a slim beam in the *xz*-plane.

When a beam is slightly bent, it can be approximately assumed that all points of its neutral axis move on a straight vertical line and consequently no displacement in the *x*-direction takes place ($u_x(z=0)=0$). Outside the neutral axis, the displacement $u_x(z\neq 0)$ is generated only by the rotation φ of the beam cross-sectional areas. For the linearized case the displacement u_z in *z*-direction is in contrast to u_x independent of the coordinate z and corresponds to the deflection curve of the beam. With the time variable t the linearized kinematic relations can be summarized as follows:

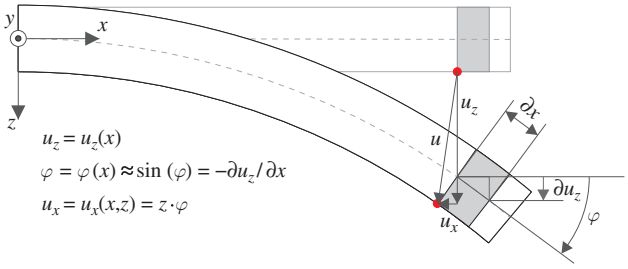

Figure 6: Linearized kinematics for the Euler–Bernoulli beam.

$$u_z = u_z(x,t) \quad u_x(x,z,t) = z\varphi(x,t)$$
$$\varphi(x,t) = -\frac{\partial u_z(x,t)}{\partial x} = -u_z' \tag{7}$$

Derivation of the State Variables

Equivalent to the passive beam the velocity v in *z*-direction and the angular velocity $\dot{\varphi}$ of the bimorph result from the kinematic relationships eq. [7]:

$$v(x,t) = \dot{u}_z \tag{8}$$

$$\dot{\varphi}(x,t) = -\dot{u}_z' \tag{9}$$

The inner bending moment at the bimorph M_b composes of the bending moment $M_{b,s}$ acting in the intermediate layer and of the two equal moments $M_{b,p}$ in the piezoelectric layers.

$$M_b(x,t) = M_{b,s} + 2M_{b,p} \tag{10}$$

In this calculation an ideal composite between the individual layers is assumed. The moments $M_{b,s}$ and $M_{b,p}$ result from the integral of the axial stress over the respective cross-sectional areas A_s and A_p. The axial stresses $T_{1,s}$ and T_1 as a function of u_z' are derived from eqs [3]–[7]. The areas A_s and A_p are the products of the bimorph width w and the height of the individual layers:

$$M_{b,s}(x,t) = \int_{A_s} T_{1,s} z \mathrm{d}A_s = \int_{A_s} \frac{1}{s_{11,s}} S_{1,s} z \mathrm{d}A_s$$
$$= \frac{w}{s_{11,s}} \int_{-\frac{h_s}{2}}^{\frac{h_s}{2}} -z^2 u_z'' \mathrm{d}z = -\frac{w h_s^3}{12 s_{11,s}} u_z'' \tag{11}$$

$$\begin{aligned} M_{\mathrm{b,p}}(x,t) &= \int_{A_\mathrm{p}} T_1 z \mathrm{d}A_\mathrm{p} = \int_{A_\mathrm{p}} \left(\frac{1}{s_{11}^\mathrm{E}} S_1 - \frac{d_{31}}{s_{11}^\mathrm{E}} E_3\right) z \mathrm{d}A_\mathrm{p} \\ &= \frac{w}{s_{11,\mathrm{s}}} \int_{\frac{h_\mathrm{s}}{2}}^{\frac{h_\mathrm{s}}{2}+h_\mathrm{p}} \left(-z u_\mathrm{z}'' \frac{d_{31}}{h_\mathrm{p}} U\right) z \mathrm{d}z \\ &= -\frac{w}{3 s_{11}^\mathrm{E}} \left(\left(\frac{h_\mathrm{s}}{2}+h_\mathrm{p}\right)^3 - \left(\frac{h_\mathrm{s}}{2}\right)^3\right) u_\mathrm{z}'' \\ &\quad - \frac{w d_{31}}{2 s_{11}^\mathrm{E}} (h_\mathrm{s}+h_\mathrm{p}) U \end{aligned} \tag{12}$$

Therewith the total bending moment is

$$\begin{aligned} M_\mathrm{b}(x,t) = &- \underbrace{\left(\frac{w h_\mathrm{s}^3}{12 s_{11,\mathrm{s}}} + \frac{2w}{3 s_{11}^\mathrm{E}} \left(\left(\frac{h_\mathrm{s}}{2}+h_\mathrm{p}\right)^3 - \left(\frac{h_\mathrm{s}}{2}\right)^3\right)\right)}_{(EI)_\mathrm{eff}} u_\mathrm{z}'' \\ &- \underbrace{\left(\frac{w d_{31}}{s_{11}^\mathrm{E}} (h_\mathrm{s}+h_\mathrm{p})\right)}_{K} U \end{aligned} \tag{13}$$

For clarity the constants $(EI)_\mathrm{eff}$ and K are introduced in eq. [13]. $(EI)_\mathrm{eff}$ corresponds to the effective bending stiffness of the entire bimorph. To calculate the shear force F the bending moment has to be differentiated with respect to x:

$$F(x,t) = \frac{\partial M_\mathrm{b}}{\partial x} = -(EI)_\mathrm{eff} u_\mathrm{z}''' \tag{14}$$

The determination of the electric current I requires an integration of the time-derived dielectric charge displacement over the electrode surface $A_\mathrm{e} = 2wl$ (IEEE (1987)).

$$\begin{aligned} I(t) &= \int_{A_\mathrm{e}} \frac{\partial D_3}{\partial t} \mathrm{d}A_\mathrm{e} = 2w \int_0^l \left(d_{31} \dot{T}_{1,\mathrm{m}} + \frac{\varepsilon_{33}^\mathrm{T}}{h_\mathrm{p}} \dot{U}\right) \mathrm{d}x \\ &= \frac{2wl}{h_\mathrm{p}} \left(\varepsilon_{33}^\mathrm{T} - \frac{d_{31}^2}{s_{11}^\mathrm{E}}\right) \dot{U} + \frac{2w d_{31}}{s_{11}^\mathrm{E}} \int_0^l -z \dot{u}_\mathrm{z}'' \mathrm{d}x \end{aligned} \tag{15}$$

A_e is equal to double the product of the bimorph width w and the length l. For a parallel bimorph this corresponds to the area the total electric charge flows through. With the relation $\int -u_\mathrm{z}'' \mathrm{d}x = \varphi$ and the average stress $T_{1,\mathrm{m}} = T_1\left(z = \frac{h_\mathrm{s}+h_\mathrm{p}}{2}\right)$, which acts in both piezoelectric layers, the electric current can be calculated as a function of the bimorph bending and the electric voltage:

$$\begin{aligned} I(t) = &\underbrace{\left(\frac{2wl}{h_\mathrm{p}} \left(\varepsilon_{33}^\mathrm{T} - \frac{d_{31}^2}{s_{11}^\mathrm{E}}\right)\right)}_{C_\mathrm{p}} \dot{U} \\ &+ \underbrace{\left(\frac{w d_{31}(h_\mathrm{s}+h_\mathrm{p})}{s_{11}^\mathrm{E}}\right)}_{K} (\dot{\varphi}(x=l) - \dot{\varphi}(x=0)) \end{aligned} \tag{16}$$

The abbreviation C_p corresponds to the capacity of the entire bimorph.

Computation of the Transfer Matrix

Based on the differential equation of motion for the Euler–Bernoulli beam, the sought state variables for a harmonic excitation (excitation frequency ω) can be determined with the Bernoulli product approach for u_z (Gasch, Knothe, and Liebich 2012):

$$\begin{aligned} v(x,t) &= e^{j\omega t} j\omega (a_1 \sin(x\lambda) + a_2 \cos(x\lambda) + a_3 \sinh(x\lambda) \\ &\quad + a_4 \cosh(x\lambda)) \\ \dot{\varphi}(x,t) &= -e^{j\omega t} j\omega (a_1 \lambda \cos(x\lambda) - a_2 \lambda \sin(x\lambda) + a_3 \lambda \cosh(x\lambda) \\ &\quad + a_4 \lambda \sinh(x\lambda)) \\ M_\mathrm{b}(x,t) &= -e^{j\omega t} (EI)_\mathrm{eff} (-a_1 \lambda^2 \sin(x\lambda) - a_2 \lambda^2 \cos(x\lambda) \\ &\quad + a_3 \lambda^2 \sinh(x\lambda) + a_4 \lambda^2 \cosh(x\lambda) - KU) \\ F(x,t) &= -e^{j\omega t} (EI)_\mathrm{eff} (-a_1 \lambda^3 \cos(x\lambda) + a_2 \lambda^3 \sin(x\lambda) \\ &\quad + a_3 \lambda^3 \cosh(x\lambda) + a_4 \lambda^3 \sinh(x\lambda)) \\ I(t) &= j\omega C_\mathrm{p} U + K(\dot{\varphi}(x=l) - \dot{\varphi}(x=0)) \end{aligned}$$

In this calculation λ is the eigenvalue of the differential equation of motion (compare Gasch, Knothe, and Liebich (2012); Cho et al. (2000)):

$$\lambda = \left(\frac{m_\mathrm{eff}}{(EI)_\mathrm{eff}} \omega\right)^{\frac{1}{4}} \tag{17}$$

λ includes the effective mass per unit length

$$m_\mathrm{eff} = w(\rho_\mathrm{s} h_\mathrm{s} + \rho_\mathrm{p} h_\mathrm{p}) \tag{18}$$

with the middle shim layer density ρ_s and the density of the piezoelectric layer ρ_p. As described by Gasch, Knothe, and Liebich (2012), the unknown coefficients a_{1-4} can be determined with the complex boundary conditions $(v_1\ \dot{\varphi}_1\ M_1\ F_1\ U)^\mathrm{T}$ and then used to calculate $(v_2\ \dot{\varphi}_2\ M_2\ F_2\ I)^\mathrm{T}$. From the resulting system of equations the transfer matrix $\boldsymbol{A}$ can be set up as follows:

$$A = \begin{pmatrix} \frac{(\cos(l\lambda)+\cosh(l\lambda))}{2} & -\frac{(\sin(l\lambda)+\sinh(l\lambda))}{2\lambda} & \frac{j\omega(\cos(l\lambda)-\cosh(l\lambda))}{2(EI)_{\text{eff}}\lambda^2} & -\frac{j\omega(\sinh(l\lambda)-\sin(l\lambda))}{2(EI)_{\text{eff}}\lambda^3} & \frac{j\omega K(\cos(l\lambda)-\cosh(l\lambda))}{2(EI)_{\text{eff}}\lambda^2} \\ \frac{\lambda(\sin(l\lambda)-\sinh(l\lambda))}{2} & \frac{(\cos(l\lambda)+\cosh(l\lambda))}{2} & \frac{j\omega(\sin(l\lambda)+\sinh(l\lambda))}{2(EI)_{\text{eff}}\lambda} & -\frac{j\omega(\cos(l\lambda)-\cosh(l\lambda))}{2(EI)_{\text{eff}}\lambda^2} & \frac{K(\cos(l\lambda)+\cosh(l\lambda)-2)}{2} \\ -\frac{j\lambda^2(EI)_{\text{eff}}(\cos(l\lambda)-\cosh(l\lambda))}{2\omega} & -\frac{j\lambda(EI)_{\text{eff}}(\sinh(l\lambda)-\sin(l\lambda))}{2\omega} & \frac{(\cos(l\lambda)+\cosh(l\lambda))}{2} & \frac{(\sin(l\lambda)+\sinh(l\lambda))}{2\lambda} & \frac{K(\cos(l\lambda)+\cosh(l\lambda)-2)}{2} \\ \frac{j\lambda^3(EI)_{\text{eff}}(\sin(l\lambda)+\sinh(l\lambda))}{2\omega} & \frac{j\lambda^2(EI)_{\text{eff}}(\cos(l\lambda)-\cosh(l\lambda))}{2\omega} & \frac{\lambda(\sinh(l\lambda)-\sin(l\lambda))}{2} & \frac{(\cos(l\lambda)+\cosh(l\lambda))}{2} & \frac{\lambda K(\sinh(l\lambda)-\sin(l\lambda))}{2} \\ \frac{\lambda K(\sin(l\lambda)-\sinh(l\lambda))}{2} & \frac{K(\cos(l\lambda)+\cosh(l\lambda)-2)}{2} & \frac{j\omega K(\sinh(l\lambda)+\sin(l\lambda))}{2(EI)_{\text{eff}}\lambda} & -\frac{j\omega K(\cos(l\lambda)-\cosh(l\lambda))}{2(EI)_{\text{eff}}\lambda^2} & \frac{j\omega\left(K^2(\sin(l\lambda)+\sinh(l\lambda))+2(EI)_{\text{eff}}C_{\text{p}}\lambda\right)}{2(EI)_{\text{eff}}\lambda} \end{pmatrix}$$

Aside from the additional fifth row and column with the electromechanical matrix elements the matrix corresponds to the transfer matrix of a passive bending beam (compare Pestel and Leckie (1963) and Richter, Twiefel, and Wallaschek (2009)). At this point it should be noted that the derived transfer matrix is only valid for the considered state variables of a parallel bimorph in the defined coordinate system. For the derivation of the transfer matrix for a serial bimorph it must be considered that E_3 and A_{e} are calculated differently:

$$E_{3,\text{serial}} = \frac{U}{2h_{\text{p}}} \qquad A_{\text{e,serial}} = wl$$

A similar derivation of the transfer matrix for a serial bimorph is made by Cho et al. (2000).

Damping

In the following the model is extended by system damping. During bimorph oscillation many factors lead to losses. One of these is the material damping, which in the model can be taken into account by a complex Young's modulus or a complex elastic compliance for the shim and the piezoelectric layers, compare to Sollmann (1981):

$$\frac{1}{s_{11}^{\text{E}*}} = \frac{1}{s_{11}^{\text{E}}}\left(1 + j\frac{1}{Q_{\text{p}}}\right) \quad [19]$$

$$\frac{1}{s_{11,\text{s}}^{*}} = \frac{1}{s_{11,\text{s}}}\left(1 + j\frac{1}{Q_{\text{s}}}\right) \quad [20]$$

The quality factor Q is a characteristic material parameter. Other mechanical damping effects, such as losses due to local friction in the bearing or the damping due to air resistance are difficult to determine separately but in the model these effects can be considered in a simplified manner by decreasing Q. In addition to the mechanical damping, there are dielectric and piezoelectric losses in the piezoelectric material. Equivalent to the complex modulus, the dielectric loss can be taken into account by a complex dielectric constant $\varepsilon_{33}^{\text{T}*}$ with the dissipation factor $\tan\delta$ and the piezoelectric loss by a complex piezoelectric constant d_{31}^{*} with the dissipation factor $\tan\theta$ as shown by Uchino and Hirosc (2001):

$$\varepsilon_{33}^{\text{T}*} = \varepsilon_{33}^{\text{T}*}(1 + j\tan\delta) \quad [21]$$

$$d_{31}^{*} = d_{31}(1 + j\tan\theta) \quad [22]$$

These assumptions are only valid for steady-state and harmonic vibrations. When applied to non-stationary oscillations non-causal system responses occur in the time-domain.

Utilization of the Bimorph Model for the Energy Harvester

To model the bimorph in the hybrid energy harvester besides the mounting conditions the solenoid unit has to be taken into account. The solenoid unit can be assumed as a passive bending beam attached at the end of the bimorph. The transfer matrix method offers a simple way to combine several passive and active elements by matrix multiplication. So the piezoelectric part of the energy harvester can be described by following equation:

$$\begin{pmatrix} v_{2,\text{passive}} \\ \dot{\varphi}_{2,\text{passive}} \\ M_{2,\text{passive}} \\ F_{2,\text{passive}} \\ I \end{pmatrix} = \text{A}_{\text{passive}}\text{A}\begin{pmatrix} v_1 \\ \dot{\varphi}_1 \\ M_1 \\ F_1 \\ U \end{pmatrix} \quad [23]$$

The passive element is attached at the bimorph end "2" (Figure 5, right). Thereby a new free end at the passive element denoted by "2,passive" results. As mentioned in section "Analytical Model of a Piezoelectric Parallel Bimorph for Steady-State, Harmonic Vibrations", the transfer matrix of a passive bending beam corresponds to the matrix $\boldsymbol{A}$ without the fifth row and column. This means that the transfer matrix for the passive element A_{passive} can be determined from the matrix $\boldsymbol{A}$ by using effective material and geometry properties of the solenoid unit and by setting all values in the fifth row and column to zero apart from $A_{\text{passive}}(5,5) = 1$.

To solve the system of eqs (23) at least five of the ten state variables must be known. $v1 = 0$ and $\dot{\varphi}_1 = 0$ results, since the bimorph end "1" (Figure 5, left) is firmly attached in the energy harvester housing. At the new free end of the

passive element no moments $M_{2,\text{passive}} = 0$ are applied. Only the magnetic force $F_{2,\text{passive}} = F_e$ induced by the rotor excites the bimorph. The Ohm's law describes the relationship between voltage and current:

$$U = ZI \qquad [24]$$

The impedance Z includes the inner resistance of the bimorph and the outer electric load. With the knowledge about the impedance Z a further state variable is eliminated. This allows to solve the system of eqs [23] and to describe the bimorph behavior.

For the validation of the bimorph model, the mechanical and electrical admittance Y_{mech} and Y_{el} of the real and modeled system are compared. Therefore, the bimorph was excited by a harmonically voltage with different frequencies. At the same time the resulting current in the bimorph and the velocity at the solenoid unit was measured. After an adaption especially of the damping parameters a very good correlation in the first mode could be achieved, see Figure 7.

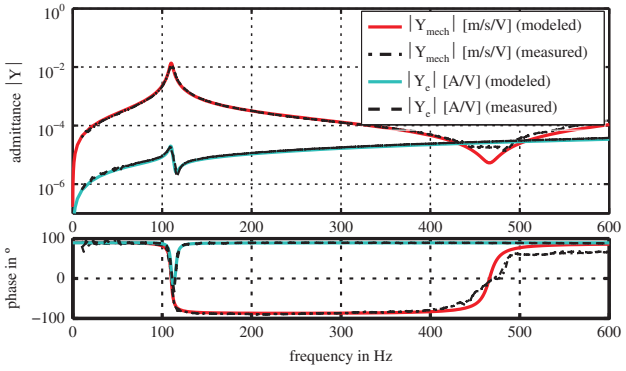

Figure 7: Comparison of the measured and modeled system behavior.

Non-harmonic Excitation Force Applied to Linear Oscillating Systems

From dynamic linear systems we know that a response function $U(t)$ is a convolution between the input variable $F_e(t)$ and the impulse response function $G(t)$. The convolution theorem states that the Fourier transform of $U(t)$ is a simple multiplication of the two Fourier transforms of $F_e(t)$ and $G(t)$:

$$U(t) = F_e(t) * G(t) \rightarrow \hat{U}(\omega) = \hat{F}_e(\omega)\hat{G}(\omega) \qquad [25]$$

Here $\hat{U}(\omega)$ is the Fourier transform of the output function, $\hat{F}_e(\omega)$ is the Fourier transform of the input function and $\hat{G}(\omega)$ is the transfer function of the system. Magnus, Popp, and Sextro (2008) state that the solution for non-harmonic excitations for mechanical systems with linear equation of motion can be found by superimposition. Therefore the algorithm for non-harmonic excitation can be divided into three steps:

1. decomposition of the input signal $F_e(t)$ into sinusoidal components
2. calculation of the response-function for each sinusoidal component separately
3. determination of the output signal $U(t)$ by superimposition of all response functions

Since we assume that the piezoelectric bimorph has linear behavior and operates in steady-state condition this principle can also be used here, as Figure 8 illustrates.

The magnetic attraction force that causes the beam oscillation (see section "Concept of a Hybrid Piezoelectric and Electromagnetic Energy Harvester" for the experimental rig) is measured by a dynamometer with N samples per revolution. Relating to a single disc revolution

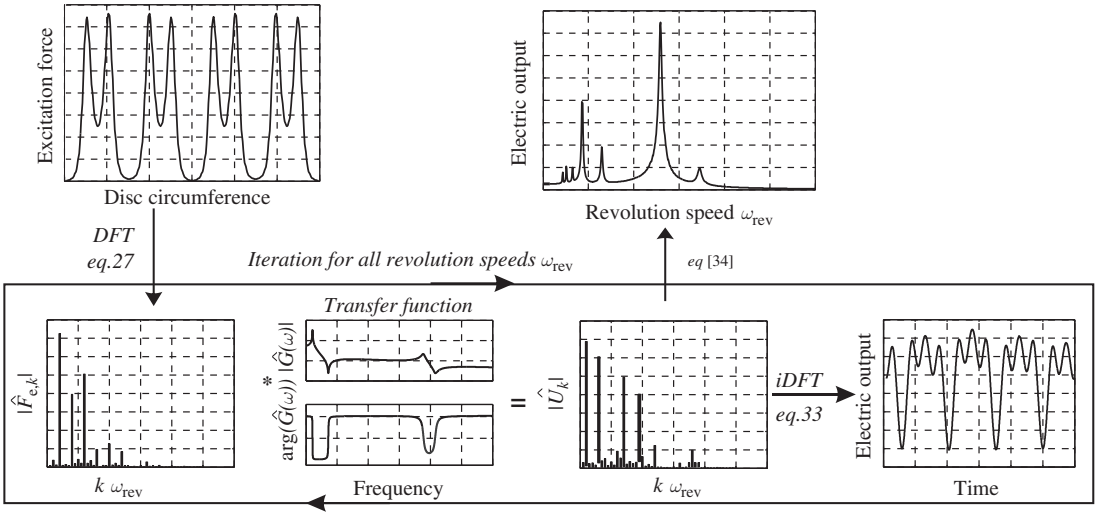

Figure 8: Sequence diagram: calculation of electric output from a non-harmonic excitation force for electromechanical systems.

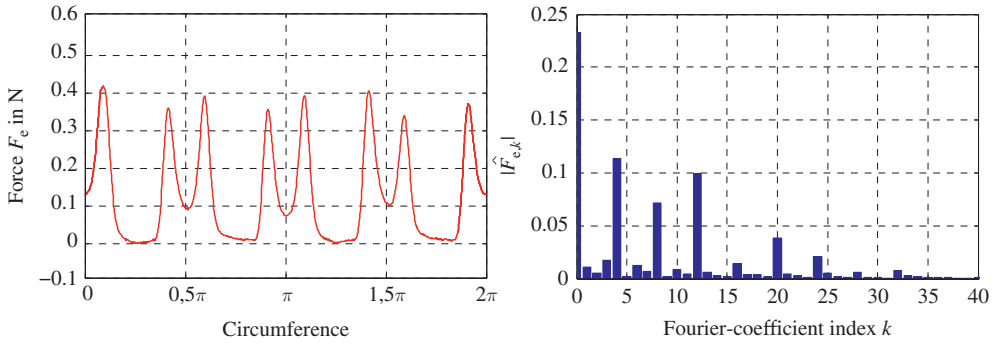

Figure 9: Waveform of the force measurement and the corresponding Fourier coefficients.

the waveform is a periodic but non-harmonic signal (Figure 9). Since the input signal is not continuous but sampled the following calculations are performed discrete. According to Butz (2001) for discrete analysis eq. (25) can be written as

$$\hat{U}_k = \hat{F}_{e,k}\hat{G}_k \qquad k = (0, \ldots, N-1) \tag{26}$$

Here $\hat{F}_{e,k}$ is a series of complex Fourier coefficients of the force-measurement respectively input signal. N is the number of samples for exactly one disc revolution, $\hat{U}_k$ are the Fourier-coefficients of the output signal and $\hat{G}_k$ are values of the transfer function at frequencies ω_k. As stated by Wang, Shen, and Chen (2012) the Fourier coefficients $\hat{F}_{e,k}$ can be calculated by discrete Fourier transformation (DFT):

$$\hat{F}_{e,k} = \frac{1}{N}\sum_{n=0}^{N-1} F_{e,n} e^{-j\frac{2\pi kn}{N}} \qquad k = (0, \ldots, N-1) \tag{27}$$

With $F_{e,n}$ as the measurement values. Each Fourier coefficient encodes the amplitude and phase of a sinusoidal component of F_e. The amplitude and phase of the sinusoidal components can be calculated from:

$$|\hat{F}_{e,k}| = \sqrt{\Re(\hat{F}_{e,k})^2 + \Im(\hat{F}_{e,k})^2} \tag{28}$$

$$\psi_{\hat{F}_{e,k}} = \arctan\frac{\Im(\hat{F}_{e,k})}{\Re(\hat{F}_{e,k})} \tag{29}$$

The frequency of those sinusoidal components is k cycles per revolution. With ω_{rev} being the revolution speed of the disc the frequency of the components is:

$$\omega_k = k\omega_{rev} \qquad k = (0, \ldots, N-1) \tag{30}$$

Therewith the series $\hat{G}_k$ can be calculated from the continuous transfer function $\hat{G}(\omega)$ by:

$$\hat{G}_k = \hat{G}(\omega_k) \qquad k = (0, \ldots, N-1) \tag{31}$$

The Fourier coefficients of the output signal now can be calculated by a multiplication of $\hat{F}_{e,k}$ with $\hat{G}_k$:

$$\hat{U}_k = |\hat{F}_{e,k}||\hat{G}_k| e^{j(\psi_{\hat{F}_k} + \psi_{\hat{G}_k})} \tag{32}$$

$\hat{U}_k$ is a series of complex Fourier coefficients of the output signal. $\hat{G}_k$ is the amplitude of the transfer function at a frequency ω_k and $\psi_{\hat{G}_k}$ is the phase of the transfer function at the same frequency.

The discrete output signal in time domain can be determined by inverse DFT. In our case $F_{e,n}$ are only real numbers, that is why the DFT of the input signal obeys the symmetry theorem. From this it follows that the coefficients with the index k and $N-k$ are complex-conjugate pairs and therefore have the same amplitude and phase. That is why the frequency spectrum $\hat{F}_{e,k}$ can be specified completely by $N/2-1$ complex numbers and a real-valued offset $\hat{F}_0$. Thereby the $\hat{U}_k$-series is also symmetrical. That is why values from $k = (0, \ldots, N/2-1)$ are summarized twice to reconstruct the output signal:

$$U_n = 2\sum_{k=0}^{N/2-1} \hat{U}_k e^{j\frac{2\pi kn}{N}} \qquad t_n = \frac{2\pi n}{\omega_{rev} N} \qquad n = (1, \ldots, N) \tag{33}$$

Here U_n is the discrete non-harmonic electric output signal in time domain with the corresponding time vector t_n. Independent from revolution speed the output signal is described by exactly N values.

The box in Figure 8 shows an illustration of the steps as aforementioned. For different revolution-speeds ω_{rev} the calculation must be performed separately from eqs [30] to [33]. Thereby the output signal waveform is varying for different speeds, as Figure 11 shows. The root mean square (RMS) values of the output signal for different revolution speeds (Figure 8) can be taken into account to evaluate the system performance. Since the Fourier-coefficients $\hat{U}_k$ are sinusoidal

components of the output signal the RMS values of the electric signals can be calculated directly from this coefficient. According to Parseval's theorem (Wang, Shen, and Chen 2012) the RMS values of the electric output are

$$U_{\mathrm{RMS}} = \frac{1}{N}\sqrt{2\sum_{k=0}^{N/2-1}|\hat{U}_k|^2} \qquad [34]$$

Electromagnetic Solenoid

According to Faraday's law of induction the induced voltage U_i is caused by a magnetic flux density $\vec{B}$ inside a solenoid:

$$U_i = -\frac{\partial\Phi}{\partial t}w_{\mathrm{sol}} \qquad \text{and} \qquad \Phi(h) = \vec{B}\vec{S} \qquad [35]$$

Here Φ is the total magnetic flux inside the solenoid, $\vec{S}$ is the vector area of the solenoid and w_{sol} is the number of windings. $\vec{B}$ is the averaged value of the non-homogeneously distributed magnetic flux density across the area $\vec{S}$. With $\vec{S}$ being oriented in e_z-direction and moving in parallel to the magnets surface only the axial component B_z of the flux density does matter for induction. Due to scattering losses in the core material and a highly nonlinear permeability usually a numerical calculation is performed. As in this article analytical solutions are provided as far as possible, it is assumed that the solenoid is air-cored and that effects of inductive coupling can be neglected. Thus the performed calculations are taken to estimate the minimum number of windings and a minimum surface area. The expected induction voltage is bigger since the core material has got high permeability. Therefore the simulation values have to be scaled by a correction factor, which is determined from measurements. Laborenz et al. (2010) describe how the radial components of the magnetic flux density of cylindrical permanent magnets can be approximated analytically. Basic approach is the magnetic vector potential $\vec{A}$, which is often used in FEM. For a cylindrical permanent magnet according to Lehner (2005) the magnetic vector potential consists only of a tangential component $\vec{A} = A_\varphi\vec{e}_\varphi$. The flux density in axial direction is then given by

$$\vec{B} = \mathrm{rot}\vec{A} \quad \rightarrow \quad B_z = \frac{\partial}{\partial r}A_\varphi \qquad [36]$$

A_φ has to be calculated from elliptic integrals according to Laborenz et al. (2010). Relating the magnetic flux density of four nearby magnets to a disc circumference s eq. [35] can also be written as

$$U_{\mathrm{i}} = -\frac{\partial\Phi}{\partial t}w_{\mathrm{sol}} = -w_{\mathrm{sol}}S\frac{\partial B}{\partial s}\frac{\partial s}{\partial t} \qquad [37]$$

Here $\frac{\partial B}{\partial s}$ is the flux density gradient along disc circumference and $\frac{\partial s}{\partial t}$ is the radial speed. With r as the disc radius eq. [37] can be transformed to

$$U_{\mathrm{i}}(\omega_{\mathrm{rev}}) = -S\frac{\partial B}{\partial s}r\omega_{\mathrm{rev}} \qquad [38]$$

Here it is evident, that in contrast to the bimorph the waveform of the time-domain voltage signal is just depending on the magnetic flux gradient $\frac{\partial B}{\partial s}$. The gradient is subject to number of magnets, their size and their placement. However the induced voltage magnitude grows linear with the number of windings, surface area and revolution speed.

Coupling Effects

The coupling effects between the two transducers can be divided into an electric coupling effect (caused by the electric connected of the transducers) and an electromechanical coupling effect (caused by Lenz law). The electric coupling effect can be avoided by preventing the charge flow between the transducers. Therefore either the transducers should be connected to separate loads or an electric wave rectifier should be installed, as shown in Figure 10. In this paper the transducers are always connected to separate loads.

The electromechanical coupling effect can be determined from measurements. Therefore the power output of one transducer is measured separately while the other is either in short-circuit or in open-loop condition. Measurements on an experimental setup, as shown in Figure 4, have led to the assumption that the electromechanical coupling effect is negligible. The differences in power output between the operation modes are so small

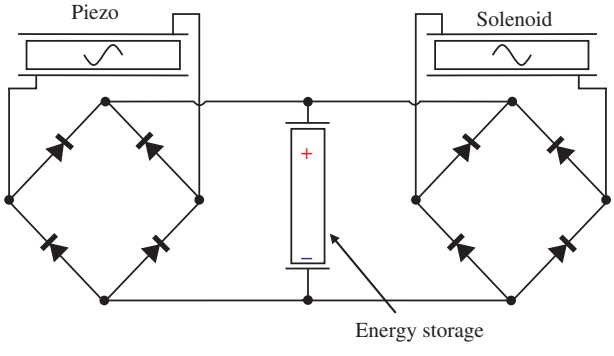

Figure 10: Wave rectifier circuits to avoid direct backward coupling effects between piezoelectric and electromagnetic generators.

that they can be regarded as being within the accuracy of a measurement. Thereby the electromechanical coupling is not considered in the model.

Analysis

In this analysis the open-electrode voltage is used as a reference to compare the time domain signals and therewith the systems dynamics of the model and the prototype device. For the bimorph Figure 11 shows the simulated versus the measured voltage signals in time domain during one revolution period for three exemplary chosen revolution speeds. The simulation data is a reconstruction from the transfer function and the excitation force as described in section "Modeling". As electric boundary condition the load impedance Z_{load} is set to infinity, this is equal to open-electrode condition. It is evident that the simulations (Figure 11 red) can reproduce the real system behavior (Figure 11 blue) almost exactly. From the Fourier coefficients on the bottom of Figure 11 and from the signals theirself it can be seen that the rate of higher harmonic oscillations in the simulated signal is marginally overrated. Since there are four magnets on circumference of the disc the dominant Fourier coefficient index is $k = 4$. Therefore the Fourier coefficients are normalized to this value. From this it can be followed that at higher bending modes the calculated transfer function differs slightly more from the real system. However at lower frequencies it matches the system almost exactly.

Figure 12 shows a comparison between the measurement of open-electrode induction voltage from the solenoid and a calculation at a certain rotation speed. It is evident that both waveforms are very similar, this is a proof for a correct solenoid model. The magnitude of the

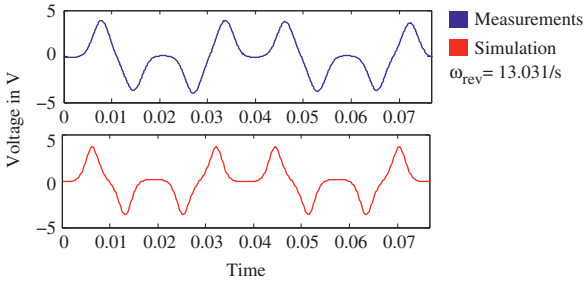

Figure 12: Comparison between simulation data and measurements of the open-electrode voltage at the solenoids electrodes. Simulation data is scaled to measurements magnitude.

measured voltage signal is bigger as the real system has got a high permeability core, which increases the magnetic flux flowing through the solenoid. Comparing the RMS values of both signals a correction factor of $1,4$ is calculated. This factor is almost constant for all considered revolution speeds.

For optimization purposes of an energy-harvesting system the study of the power output for different excitation speeds and electric loads is very important. The RMS power output in this analysis is calculated from the multiplication of the current and voltage across a varying load resistance (see Figure 4 for experimental setup). Figure 13 shows a comparison of the simulation data based on the models in section "Modeling" and measurements on the prototype. Both, the bimorphs model as well as the solenoids model, show a very good agreement with the measurements. From this data it is evident that the maximum power output of the two transducers is reached at different electric loads (marked by black dotted lines in Figure 13).

The optimum load-resistance for the bimorph is $Z_{\text{opt,piezo}} = 100\ \text{k}\Omega$ and the optimum for the solenoid is reached at only $Z_{\text{opt,sol}} = 450\Omega$. Figure 14 shows the

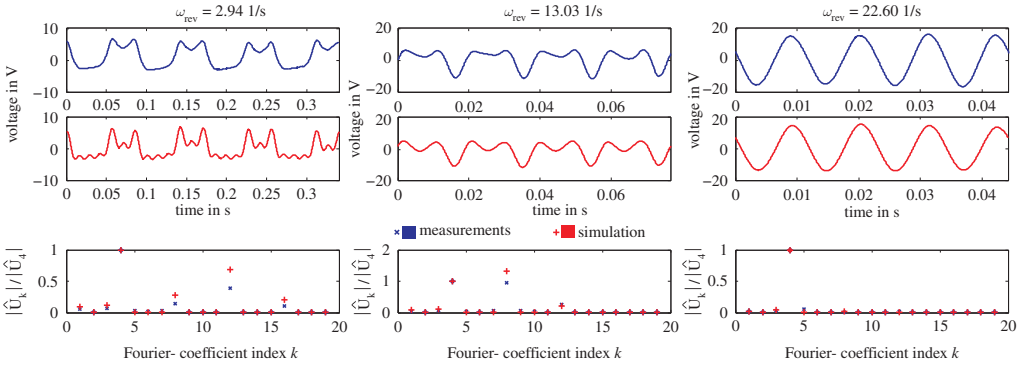

Figure 11: Comparison between simulation data and measurements of the open-electrode voltage at the bimorphs electrodes and corresponding Fourier coefficients for different revolution speeds.

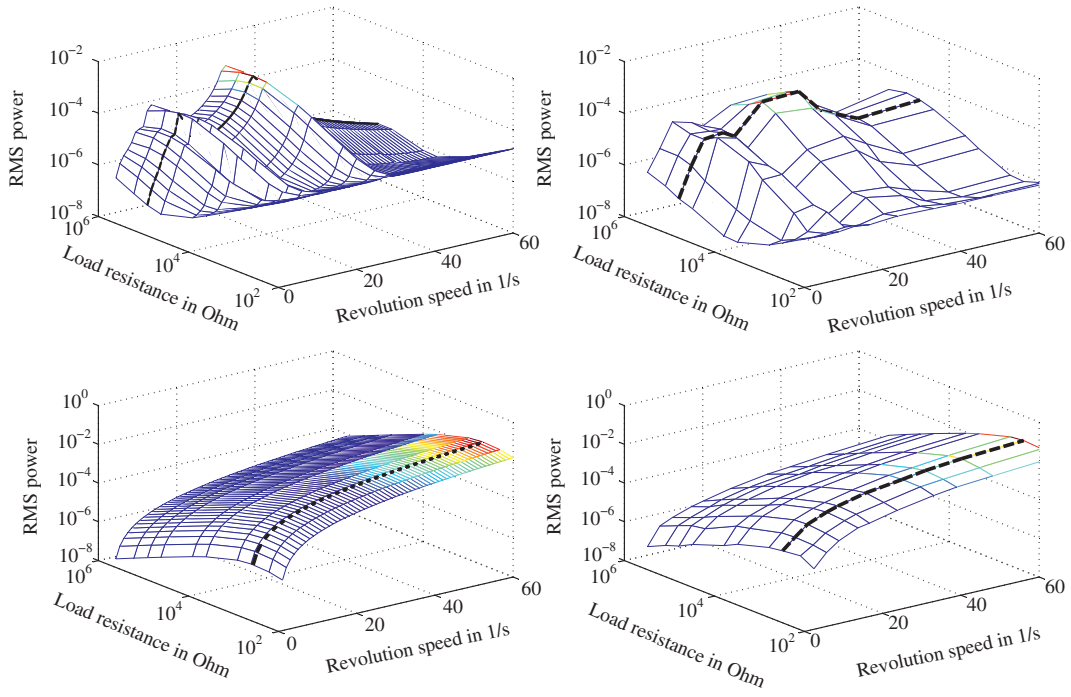

Figure 13: Comparison of power-RMS values between simulation data and measurements at the piezo-electrodes (above) and solenoid (down) for different electric loads.

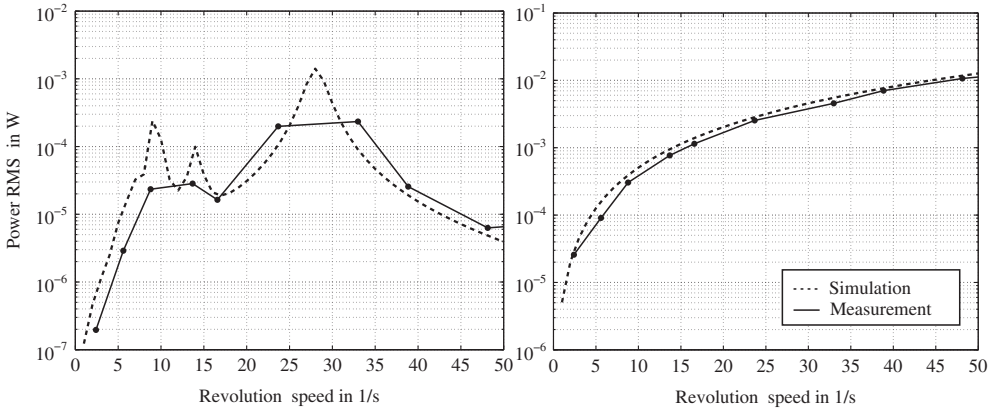

Figure 14: RMS power output at optimum electric load for the piezoelectric bimorph (left) and the solenoid (right).

comparison between RMS power output of the models and the measurements for the optimum load resistance and underline the correlation between model and measurement results. Measurements and simulation show that the solenoid provides more power at low electric loads and decreases strongly at higher loads (Figure 15). Figure 15 compares directly the simulated power output of the two transducers for different loads and excitation speeds. At higher loads and lower excitation speeds the power output of the bimorph overexceeds the power output of the solenoid.

This power compensation is the intended benefit of the hybrid concept.

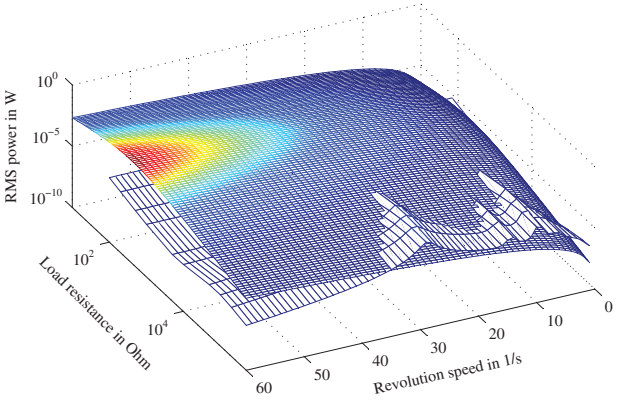

Figure 15: RMS power of the bimorph and solenoid model.

Finally, it can be stated that with our modeling approach it is possible not only to prove the performance of the prototype but also to optimize our concept for different load conditions and excitation frequencies. With a proper adjustment of the system parameters a broadband behavior can be achieved.

Conclusion

The volume of an energy-harvesting system is often limited by a defined space. In addition to this the excitation frequency and the electric load may vary with time. In this paper a modeling approach for a hybrid piezoelectric and electromagnetic energy-harvesting concept has been proposed which enables to optimize system parameter for maximum broadband energy harvesting. Therefore a brief overview of existing piezoelectric, electromagnetic and hybrid energy-harvesting concepts for rotational and vibrational energy sources was given. From this a new approach for rotating applications was developed and presented. The concept is based on a piezoelectric parallel bimorph, structural combined with a solenoid on its tip. Permanent magnets attached to a rotating object excite the bimorph and induce a voltage into the solenoid. Since the magnetic attraction force is non-harmonic, a method was submitted, which allows to determine the electric output of the bimorph by Fourier transformation and superimposition. For the bimorph an analytical model in the form of a compact transfer matrix is derived. The model is based on the Euler–Bernoulli beam theory and considers the piezoelectric coupling as well as the multilayer aspects of a bimorph. Compared to a FEM calculation, this method offers a reduced computation time, quick investigation of load influences as well as a simple way to combine several passive and active elements by matrix multiplication.

The calculated electric output signals of the bimorph and of a simple modeled solenoid have been compared to measurements of a prototype device. The comparison of these signals has shown that the simulation matches the measurements almost exactly and thus the modeling can be used to optimize the device in future. The RMS values of the power output, which depend on revolution speed and electric load, were measured and simulated to evaluate the frequency-domain performance of the device. The concept shows a broadband behavior and an equalization of the power drops over a stand-alone piezoelectric vibration harvester, which is a primary goal in energy-harvesting research. Thus the concept is ideal for application with highly fluctuating revolution speeds.

References

Beeby, S. P., R. N. Torah, M. J. Tudor, P. Glynne-Jones, T. O'Donnell, C. R. Saha, and S. Roy. 2007. "A Micro Electromagnetic Generator for Vibration Energy Harvesting." *Journal of Micromechanics and Microengineering* 17:1257–65.

Beeby, S., M. Tudor, and N. White. 2006. "Energy Harvesting Vibration Sources for Microsystems Applications." *Measurement Science and Technology* 17:175–95.

Bressers, S., D. Avirovik, M. Lallart, D. Inman, and S. Priya. 2011. "Contact-Less Wind Turbine Utilizing Piezoelectric Bimorphs with Magnetic Actuation." In *Structural Dynamics*, edited by T. Proulx, vol. 3, Conference Proceedings of the Society for Experimental Mechanics Series 233–43. New York: Springer.

Butz, T. 2001. *Fourier transformation für Fußgänger*. Wiesbaden: Vieweg + Teubner Verlag.

Challa, V. R., M. G. Prasad, and F. T. Fisher. 2009. "A Coupled Piezoelectric–Electromagnetic Energy Harvesting Technique for Achieving Increased Power Output through Damping Matching." *Smart Materials and Structures* 18. 095029.

Challa, V. R., M. G. Prasad, Y. Shi, and F. T. Fisher. 2008. "A Vibration Energy Harvesting Device with Bidirectional Resonance Frequency Tunability." *Smart Materials and Structures* 17. 015035.

Cho, Y. S., Y. Pak, C. S. Han, and S. K. Ha. 2000. "Five-Port Equivalent Electric Circuit of Piezoelectric Bimorph Beam." *Sensors and Actuators* 84:140–8.

Gasch, R., K. Knothe, and R. Liebich. 2012. *Strukturdynamik - Diskrete Systeme und Kontinua*. Berlin: Springer.

IEEE 1987. "IEEE standard on piezoelectricity." *IEEE Std. 176–1987*.

Jung, H.-J., I.-H. Kim, D. Min, S.-H. Sim, and J.-H. Koo. 2013. "A Hybrid Electromagnetic Energy Harvesting Device for Low Frequency Vibration." In *SPIE Proceedings, Active and Passive Smart Structures and Integrated Systems*, edited by H. A. Sodano, vol. 8688. 10.1117/12.2010014

Karami, M. A., J. R. Farmer, and D. J. Inman. 2012. "Nonlinear Dynamics of the Bi-stable Piezoelectric Wind Energy Harvester." In SPIE Proceedings, Active and Passive Smart Structures and Integrated Systems, edited by H. A. Sodano, vol. 8341. 10.1117/12.915722.

Laborenz, J., C. Siewert, L. Panning, J. Wallaschek, C. Gerber, and P.-A. Masserey. 2010. "Eddy Current Damping: A Concept Study for Steam Turbine Blading." *Journal of Engineering for Gas Turbines and Power* 132(5). 052505.

Lehner, G. 2005. *Elektromagnetische Feldtheorie: Für Ingenieure und Physiker*. New York: Springer.

Magnus, K., K. Popp, and W. Sextro. 2008. *Schwingungen*. Wiesbaden: Vieweg + Teubner Verlag.

Pestel, E., and F. Leckie. 1963. *Matrix Methods in Elastomechanics*. New York: McGraw-Hill Book Company, Inc.

Priya, S. 2005. "Modeling of Electric Energy Harvesting Using Piezoelectric Windmill." *Applied Physics Letters* 87. 184101

Richter, B., J. Twiefel, and J. Wallaschek. 2009. "Piezoelectric Equivalent Circuit Models." In *Energy Harvesting Technologies*: 105–28, edited by S. Priya, and D. J. Inman, New York: Springer.

Roundy, S., and P. Wright. 2004. "A Piezoelectric Vibration Based Generator for Wireless Electronics." *Smart Materials and Structures* 13:1131–42.

Sollmann, H. 1981. "Berechnung von erzwungenen, gedämpften Biegeschwingungen mit Übertragungsmatrizen." *Technische Mechanik* 2:2.

Spreemann, D., Y. Manoli, B. Folkmer, and D. Mintenbeck. 2006. "Non-resonant Vibration Conversion." *Journal of Micromechanics and Microengineering* 16:169–73.

Uchino, K., and S. Hirosc. 2001. "Loss Mechanisms in Piezoelectrics: How to Measure Different Losses Separately." *IEEE Transactions on Ultrasonics, Ferroelectrics, and Frequency Control* 48:307–21.

Wang, Y.-J., S.-C. Shen, and C.-D. Chen. 2012. "Wideband Electromagnetic Energy Harvesting from a Rotating Wheel." In *Small-Scale Energy Harvesting*: 161-82, edited by M. Lallart, InTech. 10.5772/50739.

Wurz, M., G. Kleyman, and J. Twiefel. 2013. "Highly-Integrated Energy Harvesting Device for Rotational Applications Utilizing Quasi-Static Piezoelectric and Electromagnetic Generators." In SPIE Proceedings, Active and Passive Smart Structures and Integrated Systems, edited by H. A. Sodano, vol. 8688. 10.1117/12.2012256.

Xing, X., J. Lou, G. Yang, O. Obi, C. Driscoll, and N. Sun. 2009. "Wideband Vibration Energy Harvester with High Permeability Magnetic Material." *Applied Physics Letters* 95. 134103.